A High-Resolution Global Analysis of Ocean Surface Vector Wind Merged from Scatterometers and Passive Microwave Radiometers (1987 onward). Part II: Confidence and Sensitivity Analysis

Lisan Yu* and Xiangze Jin

Woods Hole Oceanographic Institution, Woods Hole, MA 02543

Key points:

1. Errors in the retrievals need to be specified in constructing the time series.
2. An ensemble error perturbation approach is developed.
3. High winds and rain are shown to be the leading sources of uncertainty.

Running title: Confidence and sensitivity analysis

* Corresponding author: Dr. Lisan Yu, Department of Physical Oceanography, MS#21, Woods Hole Oceanographic Institution, Woods Hole, MA 2543. Email: lyu@whoi.edu

Abstract

This Part II study addresses the uncertainty assessment of the high-resolution global analysis of ocean-surface vector winds (1987 onward) by the Objectively Analyzed air-sea Fluxes (OAFlux) project. The time series was constructed from objective synthesis of 12 satellite sensors using a variational approach to find a best fit to input data in a weighted least-squares cost function. Theoretically, the weights are inversely proportional to error covariances of data. In reality, error covariances cannot be perfectly known and so the best-fit of the cost function is sensitive to the uncertainty of the weight assignment.

We present here our efforts in seeking (i) a practical use of independent buoy measurements to determine weight assignment and (ii) a feasible representation of the impacts of the weight-assignment uncertainty on the resultant vector wind analysis. In doing so, we implemented weight selection criteria that require the selected weights to make the best-fit of the cost function to be as close as possible not only to input satellite observations but also to in situ buoy measurements at 126 locations that were not included in the synthesis. We further designed an ensemble-based weight perturbation experiment to generate an ensemble of the best-fits in response to randomized weights and to use the ensemble statistics as a measure of the uncertainty of the best-fit due to the weight-assignment uncertainty. The study shows that the weight perturbation experiment is capable of identifying the leading sources of uncertainty in the OAFlux wind analysis: high winds and rain conditions.

Key words: remote sensing of ocean surface winds, scatterometer, passive microwave radiometer, error analysis.

1. Introduction and background

A high-resolution global analysis of ocean-surface vector winds from 1987 onward has been recently developed by the Objectively Analyzed air-sea Fluxes (OAFlux) project through objective synthesis of 12 satellite wind sensors [*Yu and Jin* 2014, JGR, revised; hereafter Part I]. Among the 12 satellite sensors in use, there are 2 scatterometers, namely, the SeaWind scatterometer on the NASA's QuikSCAT mission (June 1999 – November 2009) and the Advanced Scatterometer (ASCAT) that was operated by the European Organisation for the Exploitation of Meteorological Satellites (EUMETSAT) aboard the MetOp–A satellite (October 2006 onward). There are 10 passive microwave radiometers, with 6 sensors from the Special Sensor Microwave Imager (SSM/I) that was carried aboard Defense Meteorological Satellite Program (DMSP) satellites F08, F10, F11, F13, F14, and F15 (1987 onward), 2 sensors from the DMSP's Special Sensor Microwave Imager/Sounder (SSMIS) aboard satellites F16 and F17, the Advanced Microwave Scanning Radiometer - Earth Observing System (AMSR-E) sensor on NASA's Aqua satellite (May 2002 – October 2011), and the passive polarimetric microwave radiometer from WindSat aboard the joint Department of Defense (DoD)/Navy platform Coriolis mission in January 2003.

A variational approach was developed from the theory of least-variance linear statistical estimation [*Lorenc* 1986; *Daley* 1991; *Talagrand* 1997] to construct the wind speed (w), and the zonal (u) and meridional (v) wind components that best fit all input data (satellite observations, reanalysis wind components, and *a priori* terms) in a least-squares sense. Two a priori conditions were imposed, requiring that (i) the analyzed wind speed $w=sqrt(u^2+v^2)$ to be as close as possible to satellite wind speed retrievals, and (ii) the analyzed (u,v) to satisfy the kinematic constraints such as vorticity and divergence conservations. Surface vector winds from two atmospheric reanalyses served as the background information for *u* and *v*. The two reanalysis wind products were the European Centre for Medium-Range Weather Forecasts (ECMWF) Re-Analysis (ERA) interim (hereafter ERA-Interim) project [*Dee et al*. 2011] and the Climate Forecast System Reanalysis (CFSR) from the National Centers for Environmental Prediction (NCEP) [*Saha et al.,* 2010]. The two reanalyses have improved characterization of the global ocean surface winds over other reanalysis wind products when compared to buoy measurements [e.g. *Yu and Jin* 2012].

One prerequisite for all applications based on the least-variance linear statistical estimation theory is the *a priori* specification of the weight (i.e., an inversion of error covariance) for each dataset used in the cost function so that the errors in data can be accounted for during the search of a solution [*Talagrand 1999*]. In reality, those error statistics can neither be perfectly known nor be accurately specified, rendering the optimality of such framework to be dependent on the ability to obtain the most appropriate representation of error statistics [*Courtier et al.* 1994; *Wahba et al.* 1995; *Desrozier and Ivanov* 2001]. Two questions were thus raised for the OAFlux vector wind analysis. One is how to provide the best possible weight assignments for all the input data, and the other is how to quantify the degree of uncertainty in the resultant vector wind estimates caused by the uncertainty in the weight assignments. This part II analysis is to address these two issues.

Extensive efforts have been made to identify, characterize, and quantify the errors in satellite wind measurements using a variety of reference platforms, including in situ buoys, research vessels, and atmospheric reanalyses [e.g., *Ebuchi et al.* 2002; *Bourassa et al.* 2003; *Vogelzang et al.* 2011]. There are two general sources of error in satellite observations. One is measuring instrumentation noise that results from random errors of the observing system. For scatterometer retrievals, ambiguity selection errors are regarded as measurement errors [e.g. *Hoffman* 1984; *Freilich* 1997; *Stoffelen* 1998; *Bourassa et al.* 2003]. The other is representation errors [e.g. *Stoffelen* 1998; *Schlax et al.* 2000; *Bourassa and Ford* 2010; *Vogelzang et al.* 2011; *Fangohr and Kent* 2012] that are associated with unresolved spatial/temporal scales, approximations in the geophysical model functions (GMF) that relate backscatter to wind vector, and approximations in radiative transfer models (RTM) that relates emissivity to wind speed. The representation of the wind retrievals at high wind speeds is one example of representation error. The presently large uncertainties in high wind retrievals are attributable to the lack of high wind measurements from buoys or research vessels to validate the empirical assumptions in the GMFs and/or RTMs [e.g. *Fangohr and Kent* 2012; *Yueh et al.* 2001]. Rain is another source of bias for Ku-band scatterometer retrievals. Removing the rain-contaminated wind vector cells in QuikSCAT can lead to a large-scale bias in wind derivative fields [e.g. *Milliff et al.* 2004], elucidating that representation errors can have both a bias and a random component [e.g. *Bourassa and Ford* 2010].

Representation errors together with measurement errors constitute the error covariance for data constraints. However, two additional sources of error need to be considered when estimating the cost function that included not only 12 different sensors but also atmospheric reanalyses as the background fields. One error source is the model errors (biases) in the atmospheric reanalyses, and the other is the interpolation or mapping error that arises when merging satellite measurements made at discrete times onto the selected temporal resolution of equal interval. For instance, each sensor provides two daily passes, one as the orbit ascends and the other as the orbit descends. As the number of available sensors (and so the total daily passes) changes constantly with time (see Figure 1 in Part I) from 1987 to the present, the underrepresentation of sub-daily variability in the resultant daily-mean synthesis could be a source of error.

In part I, we reported that the most challenging situation for the OAFlux synthesis is the construction of the near-surface circulation associated with synoptic weather storms that feature both high winds (>15 ms^{-1}) and rain conditions. Three factors contribute to the challenge. One is the lack of passive microwave radiometer wind speed retrievals in rain conditions, which reduces satellite data coverage for the synoptic weather systems. The second is that the removal of the rain contaminated wind vector cells in QuikSCAT creates data voids that cannot be easily filled by the reanalysis winds because of the smooth spatial variability in the latter. The third factor is that wind retrievals from the C-band ASCAT [*ASCAT Wind Product User Manual*, 2013] and Ku-band QuikSCAT [*Ricciardulli and Wentz*, 2011] differ at high wind (>15 ms^{-1}) due primarily to the lack of in situ buoy validation of the GMFs at these conditions [e.g. *Dunbar et al.* 2006; *Fangohr and Kent* 2012; *Bentamy et al*. 2012]. The differences are difficult to reconcile particularly when a fast-moving synoptic system is involved. The sensitivity experiments in Part I showed that the synoptic features associated with the weather systems are scatterometer-dependent, suggesting that inter-scatterometer differences are a source of representation error for the synthesis.

The statistically-based objective approaches are not expected to mitigate the impacts of satellite technical difficulties during the synergy of sensors from multiple platforms. These approaches are capable of reducing random errors (noises) within given retrievals and searching for a solution that best fits the data constraints and the *a priori* information within the pre-described weights; but they are unable to generate an improved estimate in the presence of missing or biased retrievals and unable to remove the biases associated with representation errors due to either satellite observations, or atmospheric reanalysis winds, or mapping. Therefore, the objective synthesis is subject to the specification of error statistics (or weights) for both random and representation components. However, despite the extensive progresses that have been achieved in understanding and quantifying the representation errors of satellite and reanalysis winds [e.g. *Stoffelem* 1998; *Ebuchi et al.* 2002; *Bourassa et al.* 2003; *Vogelzang et al.* 2011; *Yu and Jin* 2012] and in employing a bias correction scheme to data assimilation to reduce the effect of biases on atmospheric reanalysis [e.g. *Desroziers and Ivanov* 2001; *Dee* 2005], not all error sources are well estimated. For example, it is usually assumed that the errors between sensor themselves and between the sensors and atmospheric reanalyses are uncorrelated. In reality, sensors are calibrated against each other [e.g. *Stoffelen and Anderson 1997*; *Ricciardulli and Wentz*, 2011], and ERA-interim and CFSR both assimilate scatterometer observations [e.g. *Dee et al.* 2011; *Saha et al.* 2010]. Given the complexity of the sources contributing to errors, it is legitimate to regard the present knowledge of errors as the best "estimate" of the errors but not the true value. This leads to the reality that no matter what the weights are assigned, there is a degree of uncertainty in the assignment and consequently, in the solution.

We introduce here our efforts in seeking (i) a practical use of existing observations for providing weight assignment and (ii) a feasible representation of the uncertainty of the weight and its impact on the resultant vector wind analysis. We designed a weight-selection experiment to find the weights that make the minimum of the cost function to be as close as possible to not only input satellite observations but also in situ buoy measurements at 126 locations that were not included in the synthesis (section 2). We further designed an ensemble-based weight perturbation experiment to generate an ensemble of the solutions in response to randomized weights and to use the ensemble statistics as a measure of the uncertainty of the solution due to the uncertainty of the weight assignment (section 3). The study shows that the weight perturbation experiment is capable of identifying the leading sources of uncertainty in the OAFlux wind analysis: the high winds and rain conditions. Nevertheless, the sources of error in input satellite and also background datasets are complex and often intercorrelated. A realistic definition of the error covariance matrices, and hence the weights, is perceived as a matter of permanent and various efforts for all applications of least-variance linear statistical estimation [*Dee* 2005; *Sadiki and Fisher* 2005; and *Bannister* 2007], no matter whether the applications are the 3D-VAR or 4D-VAR data assimilation in numerical weather prediction system [e.g. *Wahba et al.* 1995; *Courtier et al.* 1998] or the variational approach used to produce gridded products from combining various observations [*Legler et al.* 1989; *Hoffman et al.* 2003; *Atlas et al.* 2011; *Yu and Jin* 2014]. We regard this study as our first efforts toward improving the characterization and quantification of the uncertainty in the OAFlux vector wind analysis associated with the weight assignment errors. Summary and discussion are included in section 4.

2. The weight selection experiments

2.1 The cost function

As described in Part I, the cost function formulated for the OAFlux multi-sensor synthesis is expressed as follows:

$$F = \underbrace{\frac{1}{2}(\vec{V}_a - \vec{V}_b)^T R_b(\vec{V}_a - \vec{V}_b)}_{\text{(I)}} + \underbrace{\frac{1}{2}(\vec{V}_a - \vec{V}_o)^T R_o(\vec{V}_a - \vec{V}_o)}_{\text{(II)}} + \underbrace{\frac{1}{2}(w_a - w_o)^T S_o(w_a - w_o)}_{\text{(III)}}$$

$$+ \underbrace{\gamma(\nabla \times \vec{V}_a - \nabla \times \vec{V}_b)^2}_{\text{(IV)}} + \underbrace{\lambda(\nabla \cdot \vec{V}_a - \nabla \cdot \vec{V}_b)^2}_{\text{(V)}} \qquad (1)$$

where $\vec{V} = (u, v)$ is wind vector with zonal and meridional wind components denoted as u and v, respectively, and $w = \sqrt{u^2 + v^2}$ is wind speed. The superscript "T" denotes transpose. There are three subscripts: "a" denotes an estimate, "b" the background fields, and "o" satellite observations. The matrices R_b, R_o, and S_o are weighting matrices that theoretically are inversely proportional to the respective error covariance matrices of the background wind vector fields ($\vec{V}_b$), satellite wind vector observations ($\vec{V}_o$), and satellite wind speed observations (w_o). The parameters, γ and λ, are the scalings that control the effectiveness of the vorticity and divergence constraints.

The first three terms (I)-(III) are data constraints that represent a least-squares fitting of the analyzed zonal wind, meridional wind, and wind speed to input background and satellite data sets. The input satellite observations included SSM/I F08, F10, F11, F13, F15, SSMIS F16, F17, AMSRE, WindSat, QuikSCAT, and ASCAT. Among the 12 sensors, QuikSCAT and ASCAT have observations of zonal and meridional wind components while all others are radiometers providing only wind speed observations. The wind direction retrievals from WindSat were not included due to large uncertainties when compared to buoy measurements and QuikSCAT [*Yu and Jin* 2012]. The background fields were taken from ERA-Interim and CFSR, which provided information for (i) initializing wind direction when there are no scatterometer measurements prior to 1999, and (ii) gap-filling in regions where there are no satellite observations. The two reanalysis winds were also the background fields for the fourth and fifth terms (IV)-(V), which are the weak constraints for the vorticity and divergence. These two kinematic terms are spatial derivative constraints, which are used mainly for suppressing noises in satellite observations at the swath edges. The contribution of these kinematic terms to the minimization process is prescribed by the scaling parameters γ and λ. Readers are referred to Part I for the description of satellite sensors, download data sources, and the synthesis procedure.

The minimization process seeks an estimate of daily wind field of *u*, *v*, and *w* that satisfies the data constraints and the imposed kinematic constraints within the specified weights by using a conjugate-gradient iterative method [*Yu et al.* 2008]. As described in the Introduction, the main challenge for estimating the cost function (1) is the specification of the weight (i.e., an inversion of error covariance matrix) for each dataset [e.g. *Courtier et al.* 1994; *Wahba et al.* 1995; *Desrozier and Ivanov* 2001]. The errors in input satellite and reanalysis datasets have both random and systematic components. The variational approaches are capable of reducing random errors (noises) but not the biases [*Talagrand* 1999]. There have been various efforts in developing bias-aware weight correction methods [e.g. *Stoffelen* 1998; *Harris and Kelly* 2001; *Dee* 2005] that can estimate and correct systematic errors jointly with the variable estimates. These methods require to correctly attribute the detected bias to its source, and then to develop useful representations for the biases or for the mechanisms that cause them to develop. Because separation of different bias sources requires additional information (such as independent observations, knowledge of the underlying causes, and/or hypotheses about the error characteristics of possible sources), bias-aware correction methods may not produce the right correction if different sources produce similar biases [e.g. *Chapnik et al.* 2004; *Desroziers et al.* 2005; *Dee* 2005].

In addition to random and biases in input satellite and reanalysis winds, correlations of errors between satellites and reanalyses winds are also evidenced [e.g., *Stoffelen* 1998; *Frehlich* 2011; *Vogelzang et al.* 2011; *Vogelzang and Stoffelen* 2012; *Bonavita* 2012]. Existing knowledge can help to map the basic pattern of the biases associated with some bias sources, but is insufficient to help formulate accurate representation for all bias sources, not to mention their change with seasons. Needless to say, there is a wide gap between what we presently know and what the cost function (1) needs with regard to the error covariance matrices. Therefore, our strategy is simple, which is to start from the scratch, using the basics to construct the errors and to set up a frame for future development. Our goal is straightforward, which is to develop a basic framework that enables the identification and understanding of the effect of the uncertainty of the weight assignment on the resultant vector wind analysis. Our approach is a two-step approach. We first seek for reasonable assignment for the weights from a set of weight experiments and then design an ensemble weight perturbation analysis to assess the uncertainty in the wind analysis associated with the uncertainty in the weight assignment.

2.2 Design of the weight selection experiments

This study represents our first step toward establishing a framework for systematic error modeling for the vector wind analysis using least-variance linear statistical estimation. We started with the fundamental assumptions, that is, the errors are constant and uncorrelated. The cost function (1) can be simplified as follows:

$$F = \frac{1}{2}\sum_{i=1}^{I} \alpha_i \, (u_a - u_i)^2 + \frac{1}{2}\sum_{i=1}^{I} \alpha_i \, (v_a - v_i)^2 + \frac{1}{2}\sum_{j=1}^{J} \beta_j \, (w_a - w_i)^2 + \gamma(\nabla \times \vec{V}_a - \nabla \times \vec{V}_b)^2$$
$$+ \lambda(\nabla \cdot \vec{V}_a - \nabla \cdot \vec{V}_b)^2 \qquad (2)$$

where α_i represents the weight assignment for zonal and meridional wind components, with the subscript i = 1, …, I indicating the respective input scatterometers (i.e., QuikSCAT and ASCAT) and background (i.e., ERA-interim and CFSR) data sets for wind components. The weight assignment for the wind speed term is denoted by β_j, with the subscript $j = 1, \ldots, J$ indicating the respective input satellite wind speed data sets (e.g., SSM/I F08, F10, F11, F13, F15, SSMIS F16, F17, AMSR-E, WindSat, QuikSCAT, and ASCAT).

In Part I, we indicated that the weights, β_j, associated with the wind speed constraints (term (III)), were set to be 1. The weights of the ERA-interim u and v terms were assigned to be 0.8 and those of CFSR were set to be 0.4. The scaling parameters of the kinematic constraints for vorticity and divergence, γ and λ, were fixed at 0.5. The values of these weight parameters were selected from numerous sensitivity experiments we have conducted, which can be explained using Figures

1a-b. In essence, the weight selection experiments (Fig.1a) were based on the statistics of the cost minimum with respect to both input satellite datasets and the buoy measurements at 126 locations [*Yu and Jin* 2012]. The buoy measurements (Fig.1b) were not included in estimating the cost function (2) but they were assimilated by reanalyses [e.g. *Dee et al.* 2011 and *Saha et al.* 2010]. They may be better regarded as a semi-independent reference. In designing the weight selection experiments, we utilized the fact that the minimization of the cost function (2) depends on the relative values, or the ratio, between the weights assigned to the satellites and those to the reanalyses once errors are assumed to be constant. We also assigned an equal weight to the satellite sensors, as their statistics with regard to the 126 buoy time series were comparable [*Yu and Jin* 2012]. Finally, we kept the ratio between the total weights for the satellite data constraints and the total weights for the reanalyses constraint to remain unchanged over the analysis period and determined the weight ratio from the weight selection experiments that can produce the minimum of the cost function to be as close as possible to both the satellite observations and the buoy measurements. There are 11 satellite observation constraints (i.e., 7 satellite wind speed constraints, 2 scatterometer zonal wind constraints, and 2 for scatterometer meridional wind constraints) and 4 reanalysis constraints for zonal and meridional wind components. After setting an equal weight to all satellite constraints, the weight ratio can be calculated as κ = total weights for satellite constraints/total weights for reanalysis constraints = $11/x$, where x denotes the total weights for reanalysis constraints and can be determined once the optimal κ is selected.

2.3 Results

Figure 1a shows the statistical behavior of the weight selection experiments (marked by black crosses), with respect to two measures, the wind speed root-mean-square differences

(RMSD) between the experiments and buoys (the x-axis) and the wind speed RMSD between the experiments and seven satellite sensors (i.e. SSM/I F13, SSMIS F16, F17, AMSR-E, QuikSCAT, ASCAT, and WindSat) (y-axis) (the y axis). A total of 200 experiments were conducted for the year 2008 to test the performance of the cost function in response to the weight ratio that ranges from 0.5 to 1000 (i.e., the total weights assigned to the reanalysis constraints varies from 22 to 0.01). The larger (smaller) the weight ratio, the more dominant the satellite (reanalysis) data constraints are on the minimization of the cost function. As can be seen from Figure 1a, the wind speed RMSD with regard to satellites (the y-axis) approaches 0.22 ms^{-1} as the weight ratio increases beyond 15. However, the larger the weight ratio, the farther the experiments depart away from the buoy-based RMSD (the x-axis). The smallest RMSD is 0.6 ms^{-1} when the weight ratio is at 4. Thus, the two measures suggests that an optimal weight ratio should be between 4 and 15, upon which we decided to choose κ=9. This says that the corresponding total weights for the reanalysis constraints, x, is 1.2 when the total weights for the satellite constraints are set at 11. Similar experiments were conducted to decide the partition between ERA-interim (i.e. 0.8) and CFSR (i.e. 0.4) and also to determine the scaling parameters (i.e. both set at 0.4) of the kinematic constraints to the minimization of the cost function (not shown). During the process, the buoy-based measure played a leading role in selecting the weights we used in producing the wind analysis shown in Part I.

Talagrand [1999] discussed the usefulness of the statistics of the differences between the minimum of the cost function and input observations (i.e. the so-called innovation vector) in *a posteriori* diagnostics of the estimation system, which laid a theoretical framework for *Desrozier and Ivanov* [2001] to develop an adaptive tuning of the error covariance parameters in the variational estimation. Our work here demonstrates the practical usefulness of the innovation vectors together with the independent measurements (e.g. buoys) in selecting the optimal weights for data constraints.

3. The ensemble-based weight perturbation analysis

3.1 Design of the ensemble-based weight perturbation experiment

Our weight selection experiments led to a set of weights that have the optimal statistics with respect to the buoy measurements and input satellite observations. However, details of the spatial structure and temporal variability of errors cannot be deduced due to the limited coverage of the buoy measurements. The effort was limited to the weights that are constant and represent the gross impact of the errors in data on the minimization of the cost function. As the solution of the variational estimation depends on the weight assignment, there is a need to determine the uncertainty of the wind analysis associated with the uncertainty in the weight assignment in both spatial and temporal domain. Here we present an uncertainty analysis that relies on a randomization of weights to generate an ensemble of perturbed analyses to allow for the determination of the uncertainty in the solution of the cost function from the ensemble statistics. The idea is spiritually similar to the ensemble assimilation that has been commonly used in numerical weather prediction centers to improve the determination of error statistics associated with both the model forecasts and the observations [e.g., *Houtekamer et al.* 1996; *Fisher* 2003; *Buehner et al.* 2005; *Berre et al.* 2006; *Frehlich* 2011; *Bonavita* 2012]. In particular, *Desroziers and Ivanov* [2001] and *Chapnik et al.* [2004] proposed a randomization approach that relies on a perturbation of observations to generate an ensemble of perturbed analyses to allow for *a posteriori* tuning of the error covariancs based on the ensemble statistics of perturbed analyses. Our perturbation approach differs from that of ensemble data assimilation in two fundamental ways. First, we perturb the weights, not the observations [*Evensen* 1994]. Second, we use the ensemble statistics of the perturbed analyses to determine the degree of the uncertainty of the OAFlux analysis, unlike the ensemble assimilation that uses the ensemble statistics to improve the weight assignments [e.g. *Houtekamer et al.* 1996; *Sadiki and Fisher* 2005; *Desroziers et al.* 2009].

Our approach is developed from the fact that if the weights are not known exactly and have to be assigned, then the solution obtained from the minimization process may not be unique – in a sense that the solution changes with the change of weight assignments. Hence, there will be N sets of solutions when N sets of weight assignments are given, and the statistics of the ensemble with N members can provide an uncertainty estimate to the solution of the cost function. In randomizing the weights for the N sets of experiments, one condition is applied, that is, the sum of all the weights for each experiment is equal to one:

$$\sum_{i=1}^{I} \alpha_i + \sum_{j=1}^{J} \beta_j = 1 \qquad (3)$$

The weak constraints (i.e., terms (IV) and (V)) are secondary constraints that are imposed to suppress the noises in satellite observations at the swath edges, while the uncertainty in the weight assignments associated with the data constraints (i.e. terms (I) – (III)) are the leading contributors to the uncertainty of the variational estimation. By focusing on the first three terms in (2), an analytic solution for w_a, u_a and v_a that minimizes the cost function F can be derived as follows:

$$w_a = \sum_{j=1}^{J} \beta_j w_j + \sqrt{\left(\sum_{i=1}^{I} \alpha_i u_i\right)^2 + \left(\sum_{i=1}^{I} \alpha_i v_i\right)^2} \qquad (4)$$

$$u_a = \sum_{i=1}^{I} \alpha_i u_i \Big/ \left(1 - \frac{1}{w_a} \sum_{j=1}^{J} \beta_j w_j\right) \qquad (5)$$

$$v_a = \sum_{i=1}^{I} \alpha_i v_i \Big/ \left(1 - \frac{1}{w_a} \sum_{j=1}^{J} \beta_j w_j\right) \qquad (6)$$

where the dependence of w_a, u_a and v_a on input data sets w_i, u_i and v_j, as well as on weights α_i and β_j, is obtained. Once N sets of weight assignments are obtained by randomization, the resultant N sets of the solution for w_a, u_a and v_a are then used to quantify the uncertainty of w_a, u_a and v_a associated with the weight assignment uncertainty, which can be expressed in terms of the standard deviation (STD):

$$\sigma_W = STD(w_{a,n}) \quad (7a)$$

$$\sigma_u = STD(u_{a,n}) \quad (7b)$$

$$\sigma_v = STD(v_{a,n}) \quad (7c)$$

where $n = 1, \ldots N$, denoting the N sets of the solution corresponding to N sets of weight assignments.

To assess how many weight perturbation experiments are needed, we ran N from 1 to 160. Figure 2 shows the change of the globally averaged σ_w, σ_u, and σ_v with the number of experiments using the year 2008 as an example. It appears that the ensemble statistics approach a quasi-steady state when N is around 40, and further increase of the number of weight perturbation experiments does not alter the statistics as the degree of freedom for errors is determined by the number of input datasets and not the number of experiments. In the following analysis, the σ_w, σ_u, and σ_v computed at N=40 are used.

3.2 Deriving the uncertainty in wind stress and components

Once the uncertainties in wind speed, zonal and meridional components are determined, the uncertainties in wind stress, τ, zonal and meridional stress components, τ_x and τ_y, can be readily derived from the error propagation theory. The wind stress are computed from the bulk formula following *Fairall et al*. [2003]:

$$\tau = \rho C_d w^2 \tag{8a}$$

$$\tau_x = \rho C_d w u \tag{8b}$$

$$\tau_y = \rho C_d w v \tag{8c}$$

where ρ is the density of air, C_d drag coefficient. Given the relationship between τ and w, the uncertainty of τ is related to the uncertainty of w in the following way:

$$\sigma_\tau = \sqrt{\sigma_w^2 \left(\frac{\partial \tau}{\partial w}\right)^2} = \frac{2\tau}{w}\sigma_w \tag{9}$$

Accordingly, the uncertainty of τ_x, denoted σ_{τ_x}, can be derived as follows:

$$\sigma_{\tau_x} = \sqrt{\sigma_u^2 \left(\frac{\partial \tau_x}{\partial u}\right)^2 + \sigma_v^2 \left(\frac{\partial \tau_x}{\partial v}\right)^2 + 2\sigma_{uv}\left(\frac{\partial \tau_x}{\partial u}\right)\left(\frac{\partial \tau_x}{\partial v}\right)} \tag{10}$$

The assumption that the correlation between τ_x and τ_y is negligible helps simplify Eq.(10) to the following form:

$$\sigma_{\tau_x} \approx \sqrt{\sigma_u^2 \left(\tau_x \left(\frac{1}{u} + \frac{u}{w^2}\right)\right)^2 + \sigma_v^2 \left(\tau_x \frac{v}{w^2}\right)^2} \tag{11}$$

Note that correlations between τ_x and τ_y can be significant in certain regions on certain time scales. We made the assumption here to gain a first order estimation for the wind stress components. Similarly, the uncertainty of τ_y, denoted σ_{τ_y}, can be simplified as

$$\sigma_{\tau_y} \approx \sqrt{\sigma_u^2 \left(\frac{\partial \tau_y}{\partial u}\right)^2 + \sigma_v^2 \left(\frac{\partial \tau_y}{\partial v}\right)^2} = \sqrt{\sigma_v^2 \left(\tau_y \left(\frac{1}{v} + \frac{v}{w^2}\right)\right)^2 + \sigma_u^2 \left(\tau_y \frac{u}{w^2}\right)^2} \tag{12}$$

For the special case such as $u = 0$, Eq.(11) is the same as Eq.(9) because $w = abs(v)$. Likewise, Eq.(12) is identical to Eq.(9) if $v=0$. The structure of the mean error fields computed from Eqs. (9), (11), and (12) are not discussed in the following sections, as the analysis bears similarity to that of the error fields of *w, u*, and *v*.

3.3 Results

The errors in the following discussions refer to the STD of *w, u, v* associated with the uncertainty in weight assignments (Eqs. 7a-c), unless otherwise stated. The six panels in Figures 3 show the mean fields and the estimated errors for *w, u,* and *v* over the global oceans that were averaged over 25 full years (1988-2012) of the analysis period (July 1987 onwards). The latitudinally banded structure in the annual-mean pattern of *w* reflects primarily the structure in the annual-mean pattern of *u*. Westerly winds exceeding 12 ms^{-1} are located in the 30-60 degrees north and south latitudes. The trade winds of moderate wind speeds (~ 8 ms^{-1}) dictate the broad subtropical oceans, and the doldrums near the equator are under light-wind (< 5ms^{-1}) conditions all year round. On the other hand, the annual-mean pattern of *v* differs considerably from that of *u*, showing that the meridional winds associated with the Hadley circulation are most dominant over the global scale. Larger amplitude of northerlies and southerlies are all located in regions adjacent to the eastern boundary of the basin.

Despite the pattern differences in the annual-mean fields between *u* (or *w*) and *v,* the mean error patterns are surprisingly similar between the three variables, with the largest errors appearing in the same three distinct regions: the westerly belts in the northern and southern midlatitudes (40-60°) and the Intertropical Convergence Zone (ITCZ)/South Pacific Convergence Zone (SPCZ) near the equator. Errors are small in the tropical/subtropical oceans under the influence of the trade winds. The only major difference between the three sets of mean error fields is the magnitude: errors of *u* and *v* have a similar magnitude that is evidently larger than that of the *w* error. The variation of the errors with latitudinal bands can be further seen in the zonally averaged plots in Figure 3. When averaged globally and over the 25-year period, the errors induced by weight-assignment errors are estimated to be 0.21 ms^{-1} in *w,* 0.30 ms^{-1} in *u*, and 0.32 ms^{-1} in *v.*

The 25-year averaged monthly fields in January and July are shown in Figures 4-5, respectively. Seasonal variations in *w* and *u* are characterized by the strengthening of northern (southern) hemispheric westerlies in January (July), while seasonal changes in *v* are featured by an equatorward enhancement of the southeast trades in all three tropical /subtropical basins in July. The magnitude of mean errors increases in accordance with the seasonal enhancement of prevailing winds during the respective hemisphere's winter season. For instance, large errors are located between 30-60°N in January when the Northern Hemispheric westerlies are seasonally strong, but are shifted to the latitudes between 30-60°S in July when the Southern Hemispheric westerlies are seasonally strong. Errors in the ITCZ region, particularly in the eastern tropical Pacific also become more dominant in July. The zonally averaged plots in Figures 4-5 are a good summary of the dependence of errors on the magnitude of wind speed and components. Additionally, these plots also reveal that, consistent to what has been observed in Figure 3, the errors of the three variables all have a similar latitudinal distribution but the magnitude of errors of *u* and *v* is greater than that of *w*.

3.4 Impacts of rain and high winds on error estimates

The similarity in error spatial structures between *w, u,* and *v,* despite the noted differences in the mean structure of the three variables, suggests that the errors are not controlled by the magnitude of wind speed and components. As discussed in *Yu and Jin* [2014], rain and high winds are the two major sources of uncertainty for satellite surface wind retrievals. The impacts of the two conditions on the uncertainty analysis are investigated here.

The rain flags from the SSM/I series (SSM/I F13, 16, and 17) were counted on a daily basis to form a time series of daily rain mask over the 25-year (1988-2012) period, from which the number of rain days per month was constructed. The time-mean averages for annual mean, January, and July are shown in Figures 6a-c, respectively. Frequent rain days appear in three major latitudinal bands, including the ITCZ in the tropical oceans, the north midlatitudes (30-65°N), and the southern midlatitudes (40-65°S). The latter two latitudinal bands are known to be the regions of the mid latitude storm tracks [*Hoskins and Valdes* 1990]. On average, rain is most frequent in the ITCZ/SPCZ regions, with a mean of ~ 16 days per month over most of the Pacific sector. Seasonal changes in the rain frequency are noted: there are more rain days during the boreal summer and less in the boreal winter. The rain frequency associated with the midlatitudes storm tracks also changes with seasons, typically with enhanced activity during the hemisphere's summer season. Yet, the North Atlantic appears to be an exception, as there are more rain days in January than in July, particularly along the Gulf Stream and its extension.

The number of high winds (>15ms^{-1}) days was also counted using the same SSM/I series (F13, 16, and 17). The 25-year time-mean averages for annual mean, January, and July are shown in Figures 7a-c, respectively. It is evidenced that high wind events occur predominantly at higher latitudes (poleward 40° north and south) during the hemisphere's winter season. The occurrence of high winds is less frequent than the occurrence of rain, which is averaged about than 10 days per month during the winter season.

Seasonal variations of the number of rain days and high-wind days are summarized by the plots of the zonal averages in Figures 8a-b. To evaluate their respective connection to the estimated error structures in wind speed and components, the plots of the zonally averaged errors of *w, u,* and *v* are included in Figures 8c-e. One feature is clear: in the tropical oceans where winds are relatively weak, the uncertainty in wind estimates correlates primarily with the rain frequency. On the other hand, in the extratropical regions where winds are subject to strong influence of mid-latitude storms, rain and high wind conditions are equal contributors to errors in wind estimates. Take the North Atlantic as an example. The frequent rain days and high-wind days in January (Figs. 6b&7b) cause large errors in all components. Winter storms bring along not only powerful winds but also heavy precipitation. Under storm conditions, even without rain, the differences between sensors at high wind speeds [*Yu and Jin* 2014] are significant and can result in uncertainty in wind estimates. With rain in sight, the uncertainty is even greater. Rain affects all microwave sensors in various degrees depending on the frequency [*Meissner and Wentz* 2009; *Portabella and Stoffelen* 2001; *Portabella et al.* 2012; *Stile and Yueh* 2002; *Weissman et al.* 2002; 2012]. Microwave radiometers are highly sensitive to rain and thus provide no retrievals in rain conditions. QuikSCAT is sensitive only to heavy rain (i.e., vertically integrated rain rate greater than 2.0 km mm hr^{-1}), while ASCAT is not affected directly by rain. The removal of rain contaminated wind retrievals in QuikSCAT leads to data voids. Reanalyzed winds are the default background fields, but the differences between models and satellites under extreme conditions often do not help to alleviate the problem.

3.5 Why are errors of *u* and *v* larger than errors of *w*?

The error generation in *w, u*, and *v* under high winds and rain conditions is examined in Figures 9-10 using the daily fields on 01 January 2005. The rain rate retrievals are derived from SSM/I F13 (Fig.9a), in which narrow bands of rain are evident in regions of convective rain belts of the ITCZ and SPCZ and also in mid-latitudes associated with synoptic storms. The daily averaged near-surface wind speed fields from SSM/I F13 (Fig.9b) and QuikSCAT (Fig.9c) show that winds are relatively weaker (<8ms^{-1}) in the tropics but tend to be highly variable in the extratropical oceans, where bands of strong winds (>15ms^{-1}) can appear either in the neighborhood of rain bands (e.g. the North Pacific) or with no rain in presence (e.g. the North Atlantic). It is evident that the SSM/I wind speed field has more missing values due to both rain and diamond-shaped coverage gaps. The QuikSCAT field has less missing values as the coverage is greater and the sensor is sensitive only to heavy rain.

On that day, there are seven sensors (SSM/I F13, F14, F15, F16, AMSRE, WindSat wind speed, QuikSCAT) that can be used for the synthesis. The resultant synthesized fields of *w*, *u*, and *v* are shown in Figures 10a-c, and the corresponding error estimates in Figures 10d-f. The wind components fields show that higher winds in the extrotropical oceans are organized primarily around the cyclonic circulations, but the locations of strong zonal winds differ from the location of strong meridional winds. Ironically, the three error fields have a similar error pattern, which mirrors to a large extent the rain pattern in Figure 9a. Nevertheless, there is a difference in the magnitude between the three error fields. Take the North Pacific as an example. Four meridional bands of large errors of *v* lie across the region between 120°E and 140°W, each of which is about 20° long. The error bands on the two sides are associated with the local rain bands, while the middle one, along the 180 meridian, is in a rain-free area. Interestingly, we found that the contributor to this rain-free error band is due to the strong northerly winds (Fig. 10c). In estimating the cost function (1), the input datasets for *u* and *v* included QuikSCAT and also reanalyses from ERAinterim and CFSR. By comparison, input datasets for *w* had satellite retrievals from 7 sensors, with reanalyzed fields used only for filling in data gaps when necessary. The reanalyzed *w* fields were not used as a data constraint but the reanalyzed *u* and *v* fields were part of data constraints (e.g. term (I) in cost function (1)). Despite that their weights were assigned to be much weaker than the satellites (i.e, the ratio between the total satellite constraints and the total reanalysis constrains is 11:1.2; see Fig.1), the estimation of *u* and *v* is influenced by the background fields more than the estimation of *w*. Our sensitivity experiments in Part I have revealed that the differences between satellite and reanalyses *u* and *v* under high-wind and rain conditions are difficult to reconcile and contribute to the uncertainty of the *u* and *v* estimates. Figure 10 shows that the weight perturbation analysis is able to capture the leading source of uncertainty and produces an error pattern that is consistent with the sensitivity analysis in Part I.

3.6 Rain and high winds detected by SSM/I and QuikSCAT

Wind speed retrievals from the SSM/I series rely on the measurements made at 37 GHz channels, and wind speed and vector retrievals from QuikSCAT are made at 14 GHz. Since higher frequency bands are more sensitive to rain than lower frequency bands, SSM/I wind retrievals are more susceptible to rain than QuikSCAT. SSM/I provides no wind retrievals whenever there is rain, while QuikSCAT is only sensitive to heavy rain (i.e., vertically integrated rain rate greater than 2.0 km mm hr^{-1}). One can expect that SSM/I has more rain-flagged days than QuikSCAT. This is shown in Figures 10a-c, a comparison of the total rain amount derived from SSMI F13 with the total number of rain days derived from the respective SSM/I F13 and QuikSCAT in 2008. The difference in the sensitivity of the two sensors with regard to rain is most evident in the extratropical storm track region, where SSM/I wind retrievals have about 180 rain days in a year over the most areas (Fig.9b) while QuikSCAT wind retrievals have much less rain-flagged days except in the western boundary current regions (Fig.9c). There are more useful wind retrievals from QuikSCAT than from one SSMI sensor. Apparently, QuikSCAT has advantages over SSM/I in that it is not only capable of providing wind speed and direction information but also capable of producing more data coverage under similar rain conditions.

A comparison of the number of high-wind days derived from SSM/I with that derived from QuikSCAT is shown in Figures 12a-b, respectively. The plots were constructed using the wind retrievals in 2008. The two patterns are remarkably similar. SSM/I has slightly more high-wind days at a few spots, such as the north Atlantic near 50°N and the southern Indian Ocean near 45°S. In 2008, the northern Atlantic Ocean was under the influence of high winds for 50-60 days, while the northern Pacific and the southern Atlantic Ocean had only about 20-30 days on average. In the southern oceans, high winds are embedded within the strong westerly wind belt and are localized at sites such as the Indian and Pacific sectors with a frequency of 50-60 days per year. The high-wind frequency derived from SSMIS, ASMRE and WindSat (not shown) is similar to that from SSM/I, due mostly to the use of the same RTM in retrieving winds from these sensors and the inter-calibration between QuikSCAT and radiometers performed by the Remote Sensing Systems (http://www.remss.com).

3.7 Dependence of the estimated errors on rain intensity and wind speed

The discussions above delineated that the ensemble error statistics of *w, u,* and *v* generated by the weight perturbation analysis are capable of representing the impact of rain and high wind conditions on the OAFlux analysis. To quantify the dependence of the estimated errors of *w, u,* and *v* on rain intensity and wind speed magnitude for all ranges, the errors were binned onto the SSM/I rain rate bin of every 50 cm yr^{-1} and the SSM/I wind speed bin of every 1 ms^{-1}. It can be seen that the *w, u,* and *v* errors increase with both rain intensity and wind speed (Figs. 13a-b). For the rain rate in the range of 0 – 1000 cm yr^{-1}, the *w* errors increase from 0.2 ms^{-1} to 0.3 ms^{-1} and the *u* and *v* errors from 0.3 ms^{-1} to 0.6 ms^{-1}. The greater sensitivity of *u* and *v* estimates to rain intensity is consistent with the analysis of Fig.10, indicating the difficulty of using the reanalysis winds to fill in the rain-induced data gaps in QuikSCAT. The estimates of *w* are less affected by reanalysis because all sensors provide wind speed retrievals and have good global coverage on daily basis.

The association of the *w, u,* and *v* errors with the wind speed (Fig.13b) depicts clearly the influence of high winds. At low to moderate wind speed range (2 – 10 ms^{-1}), the errors of *w, u,* and *v* remain leveled at around 0.2 ms^{-1} for *w* and 0.3 ms^{-1} for *u* and *v*. All errors show a sharp increase when wind speed is greater than 10 ms^{-1}. For instance, when wind speed strengthens from 15 to 20 ms^{-1}, errors of *u* and *v* jump from 0.4 to 0.6 ms^{-1} and errors of *w* from 0.2 to 0.4 ms^{-1}. In general, errors of *v* are more sensitive to high wind conditions and has the largest rate of increase with wind speed.

4. Summary and discussion

A high-resolution global analysis of ocean-surface vector winds from 1987 onward has been recently developed by the OAFlux project through objective synthesis of 12 satellite wind sensors [see Part I]. The 12 satellite sensors include 2 scatterometers (QuikSCAT and ASCAT) that have wind speed and direction retrievals, and 10 passive microwave radiometers (6 SSM/I sensors - F08, F10, F11, F13, F14, and F15; 2 SSMIS sensors – F16 and F17, AMSR-E, and the passive polarimetric microwave radiometer from WindSat) that have wind speed retrievals only. This Part II study addresses the uncertainty analysis of the OAFlux vector wind time series that was constructed from using a variational approach to find a best fit to input data (satellite observations, reanalysis wind components, and *a priori* terms) in a weighted least-squares cost function. The weights are inversely proportional to error covariances of data. Since error covariances cannot be perfectly known, the best-fit of the cost function is sensitive to the uncertainty of the weight assignment.

We presented in this study our efforts in seeking (i) a practical use of independent buoy measurements to determine weight assignment and (ii) a feasible representation of the impacts of the weight-assignment uncertainty on the resultant vector wind analysis. In doing so, we implemented weight selection criteria that require the selected weights to make the best-fit of the cost function to be as close as possible not only to input satellite observations but also to in situ buoy measurements at 126 locations that were not included in the synthesis. The idea of the weight selection experiment was inspired by the study of *Desroziers and Ivanov* [2001] in that the error covariance parameters can be tuned adaptively using the diagnostics of the differences between the solution of the cost function and input observations (i.e., the innovation vectors). We demonstrated here that independent buoy measurements are an effective addition in selecting the optimal weights for the cost function. A total of 200 experiments were conducted to test the performance of the cost function in response to various weight ratios between the total weights assigned to satellite data constraints and those to reanalyses constraints, from which an optimal ratio was determined. However, details of the spatial structure and temporal variability of the errors cannot be deduced due to the limited coverage of the buoy measurements. The experiment was limited to the weights that are assumed to be constant and the selection criteria is based on the gross impact of the weights on the minimization of the cost function.

To determine the uncertainty of the wind analysis associated with the uncertainty in the weight assignment in both spatial and temporal domain, we further designed an ensemble-based weight perturbation experiment to generate an ensemble of the solutions in response to randomized weights and to use the ensemble statistics as a measure of the uncertainty of the solution due to the uncertainty of the weight assignment. A total of 160 sets of weight perturbation experiments were conducted. The ensemble statistics approach a quasi-steady state when *N* is around 40, and further increase of the number of experiments does not change the statistics as the degree of freedom for errors is determined by the number of input datasets not by the number of sensitivity experiments. When averaged globally and over the 25-year analysis period, the estimated mean STD weight assignment error is 0.21 ms^{-1} in *w,* 0.30 ms^{-1} in *u*, and 0.32 ms^{-1} in *v.*

High winds (>15ms^{-1}) and rain conditions are identified as the leading sources of uncertainty in the OAFlux wind analysis. The three error fields of *w, u,* and *v* are shown to have a similar spatial pattern, with large errors appearing in three distinct regions: the westerly belts in the northern and southern midlatitudes (40-60°) and the ITCZ/SPCZ rain belts in the tropical oceans. It is evidenced that the error patterns are not controlled by the magnitude of wind speed and components but by the patterns of high winds and rain rate. Wind retrievals from different sensors differ at high wind speeds due to the lack of the ground-based high-wind measurements as validation. The effect of rain on microwave sensors depends on the operating frequency, with QuikSCAT retrievals being contaminated under heavy rain. It is found that the removal of rain contaminated wind retrievals in QuikSCAT leads to data gaps in *u* and *v* components that cannot be filled in by reanalysis winds as the differences between satellite and reanalysis associated with strong rain storms are usually large and difficult to reconcile. This explains that errors of *u* and *v* have a magnitude larger than errors of *w*. It appears that the ensemble-based weight-perturbation analysis is capable of identifying the leading error sources in the OAFlux analysis and producing an error quantification that reflects the impact of leading error sources.

Given the complexity of the sources contributing to errors, the present analysis of errors represents the first effort we made toward improving the characterization and quantification of the uncertainty in the OAFlux vector wind analysis associated with the weight assignment errors. It appears that further reduction of the uncertainty of a multi-sensor synthesis is possible only when more scatterometers are available that allows for more global coverage and minimizes the need of reanalyses as the background datasets. Currently, the satellite ocean-wind observing system reaches a historical three-scatterometer constellation that features ASCAT aboard EUMESAT MetOP-A and -B, and the Indian OceanSat-2 scatterometer launched by ISRO. ASCAT-A and –B are less sensitive to rain and OceanSat-2 has a global daily coverage equivalent to QuikSCAT. The three scatterometers when combined present a unique opportunity to improve the understanding and estimation of the wind estimates under all weather conditions.

Acknowledgements

The project is sponsored by the NASA Ocean Vector Wind Science Team (OVWST) activities under grant NNA10AO86G. We thank the international OVWST members for their support and inputs during the five-year development of the OAFlux wind synthesis products. The satellite wind products of SSMI, SSMIS AMSRE, and QuikSCAT were downloaded from Remote Sensing Systems at http://www.ssmi.com/, and ASCAT datasets from NASA JPL PO.DAAC at http://podaac.jpl.nasa.gov. The original ASCAT datasets are hosted by KNMI at http://www.knmi.nl/scatterometer. The ERA-interim winds were from NCAR Research Data Archive at http://dss.ucar.edu and the original datasets are produced by ECMWF. CFSR winds were obtained from NCEP/CFSR data archives at NCDC NOMADS data access.

References

ASCAT Wind Product User Manual (2013). Version 1.13. May 2013. Ocean and Sea Ice SAF. 23pp. Available from http://www.knmi.nl/scatterometer/publications/pdf/ASCAT_Product_Manual.pdf.

Atlas, R., R. N. Hoffman, J. Ardizzone, S. M. Leidner, J. C. Jusem, D. K. Smith, and D. Gombos (2011). A cross-calibrated, multiplatform ocean surface wind velocity product for meteorological and oceanographic applications. *Bull. Amer. Meteor. Soc.*, **92**, 157–174. doi: 10.1175/2010BAMS2946.1.

Bannister R. N. (2007). Can wavelets improve the representation of forecast error covariances in variational data assimilation? *Mon. Weather Rev*., **135**, 387–408.

Berre, L., S. Stefanescu, and M. Belo Pereira, (2006). The representation of analysis effect in three error simulation techniques. *Tellus*, **58A**, 196–209.

Bentamy , A., S. A. Grodsky, J. A. Carton, D. Croizé-Fillon, and B. Chapron, (2012). Matching ASCAT and QuikSCAT winds. *J. Geophys. Res.,* **117**, C02011, doi:10.1029/2011JC007479.

Bonavita, M. (2012) Ensemble of data assimilations and uncertainty estimation. ECMWF Seminar on Data assimilation for atmosphere and ocean, 135-160.

Bourassa, M. A., and K. M. Ford, (2010). Uncertainty in Scatterometer-Derived Vorticity. *J. Atmos. Oceanic Technol.*, **27**, 594–603. doi: http://dx.doi.org/10.1175/2009JTECHO689.1

Buehner, M., P. Gauthier, and Z. Liu (2005). Evaluation of new estimates of background- and observation-error covariances for variational assimilation. *Quart. J. Roy. Meteor. Soc.,* **131**, 3373–3383.

Chapnik, B., G. Desroziers, F. Rabier, and O. Talagrand (2004). Properties and first application of an error statistics tuning method in a variational assimilation. *Q. J. R. Meteorol. Soc.,* **130**, 2253–2275.

Courtier, P., J.-N. Thepaut, and A. Hollingsworth (1994). A strategy for operational implementation of 4D-Var using an incremental approach. *Q. J. R. Meteorol. Soc.*, **120,** 1367–1387.

Courtier, P., E. Andersson, W. Heckley, J. Pailleux, D. Vasiljevic, et al. (1998). The ECMWF implementation of three-dimensional variational assimilation (3D-VAR). Part I: formulation. *Q. J. R. Meteorol. Soc*., **124**, 1783–1807.

Daley, R. (1991). *Atmospheric Data Analysis.* Cambridge University Press. 457pp.

Dee, D. P. (2005). Bias and data assimilation. *Q. J. R. Meteorol. Soc.,* **131**, 3323–3343.

Dee, D. P., and co-authors. (2011). The ERA-Interim reanalysis: configuration and performance of the data assimilation system. *Q. J. R. Meteorol. Soc.*, **137**, 553-597. doi: 10.1002/qj.828.

Desroziers, G. and S. Ivanov (2001). Diagnosis and adaptive tuning of information-error parameters in a variational assimilation. *Q. J. R. Meteorol. Soc.*, **127**, 1433–1452.

Desroziers, G., L. Berre, B. Chapnik, and P. Poli (2005). Diagnosis of observation, background and analysis-error statistics in observation space. *Q. J. R. Meteorol. Soc.,* **131**, 3385-3396.

Desroziers, G., L. Berre, V. Chabot, and B. Chapnik (2009). A Posteriori Diagnostics in an Ensemble of Perturbed Analyses. *Mon. Wea. Rev.*, **137**, 3420–3436. doi: http://dx.doi.org/10.1175/2009MWR2778.1

Dunbar, R., and Coauthors, (2006). *QuikSCAT science data product user manual*, version 3.0. JPL Doc. D-18053—Rev. A, Jet Propulsion Laboratory, Pasadena, CA, 85 pp.

Ebuchi, N., H. C. Graber, and M. J. Caruso (2002). Evaluation of wind vectors observed by QuikSCAT/SeaWinds using ocean buoy data. *J. Atmos. Ocean. Technol.*, **19,** 2049-2069.

Evensen, G. (1994). Sequential data assimilation with a nonlinear quasigeostrophic model using Monte Carlo methods to forecast error statistics. *J. Geophys. Res.,* **99(C5)**, 10,143–10,162.

Fairall, C. W., E. F. Bradley, J. E. Hare, A. A. Grachev, and J. B. Edson (2003). Bulk parameterization of air-sea fluxes: Updates and verification for the COARE algorithm. *J. Climate*, **16**, 571–591.

Fangohr*,* S., and E. C. Kent (2012)*.* An estimate of structural uncertainty in QuikSCAT wind vector retrievals. *J. Appl. Meteor. Climatol.,* **51**, 954–961.

Fisher, M. (2003) Background error covariance modelling. ECMWF Seminar on Recent developments in data Assimilation for Atmosphere and Ocean, 45-–63.

Frehlich, R. (2011). The definition of 'truth' for Numerical Weather Prediction error statistics. *Quart. J. R. Met. Soc.,* **137**, 84-98.

Freilich, M. H., (1997). Validation of vector magnitude datasets: Effects of random component errors. *J. Atmos. Oceanic Technol*., **14**, 695–703.

Harris, B. A. and G. Kelly (2001). A satellite radiance-bias correction scheme for data assimilation. *Q. J. R. Meteorol. Soc.,* **127**, 1453–1468.

Hoffman, R. N. (1984). SASS wind ambiguity removal by direct minimization. Part II: Use of smoothness and dynamical constraints. *Mon. Wea. Rev.*, **112**, 1829–1852.

Hoffmann, R. N., S. M. Leidner, J. M. Henderson, R. Atlas, J. V. Ardizzone, and S. C. Bloom, (2003). A two-dimensional variational analysis method for NSCAT ambiguity removal: Methodology, sensitivity, and tuning. *J. Atmos. Oceanic Technol.*, **20,** 585–605.

Hoskins, B. J., and P. J. Valdes, (1990). On the existence of storm-tracks. *J. Atmos. Sci.*, **47**, 1854–1864. doi: http://dx.doi.org/10.1175/1520-0469(1990)047<1854:OTEOST>2.0.CO;2.

Houtekamer, P., L. Lefaivre, J. Derome, H. Ritchie, and H. Mitchell (1996). A system simulation approach to ensemble prediction. *Mon. Wea. Rev.*, **124**, 1225–1242.

Kent, E. C., and P. G. Challenor (2006).Toward estimating climatic trends in SST. Part II: random errors. *J. Atmos. Oceanic Technol.*, **23**(3). 476-486. 10.1175/JTECH1844.1.

Kent, E.C., and A. Kaplan (2006). Toward estimating climatic trends in SST. Part III: systematic biases. *J. Atmos. Oceanic Technol.,* **23**(3). 487-500. 10.1175/JTECH1845.1.

Legler, D. M., I. M. Navon, and J. J. O'Brien, (1989). Objective Analysis of pseudo-stress over the Indian Ocean using a direct minimization approach. *Mon. Wea. Rev*., **117**, 709-720.

Lorenc, A. C., (1988). Optimal nonlinear Objective Analysis. *Quart. J. Roy. Met. Soc*., **114**, 205-240.

Meissner, T., and F. J. Wentz, (2009). Wind vector retrievals under rain with passive satellite microwave radiometers. *IEEE Trans. Geosci. Remote Sens.*, **47**(9), 3065-3083.

Milliff, R. F., J. Morzel, D. B. Chelton, and M. H. Freilich, (2004). Wind Stress Curl and Wind Stress Divergence Biases from Rain Effects on QSCAT Surface Wind Retrievals. *J. Atmos. Oceanic Technol.*, **21**, 1216–1231. doi: http://dx.doi.org/10.1175/1520-0426(2004)021<1216:WSCAWS>2.0.CO;2.

Portabella, M., and A. Stoffelen (2001). Rain Detection and Quality Control of SeaWinds. *J. Atm. Oceanic Technol.*, **18**, 7, 1171-1183.

Portabella, M., A. Stoffelen, W. Lin, A. Turiel, A. Verhoef, J. Verspeek, and J. Ballabrera-Poy (2012). Rain effects on ASCAT-retrieved winds: toward an improved quality control. *IEEE Trans. Geosci. Remote Sens.*, **50**(7), 2495-2506.

Quilfen, Y., B. Chapron, T. Elfouhaily, K. Katsaros, and J. Tournadre, (1998). Observation of Tropical Cyclones by High-Resolution Scatterometry. *J. Geophys. Res.,* **103**(C4), 7767-7786.

Ricciardulli, L, and F. J. Wentz (2011). Reprocessed QuikSCAT (V04) Wind Vectors With Ku-2011 Geophysical Model Function, Report # 043011, Remote Sensing Systems, Santa Rosa, CA, 8 pp.

Sadiki, W. and C. Fischer (2005). A posteriori validation applied to the 3D-VAR Arpege and Aladin data assimilation systems. *Tellus*, **57A**, 21—34.

Saha, S., and co-authors, (2010). The NCEP climate forecast system reanalysis. *Bull. Amer. Meteor. Soc.,* **91**, 1015-1057. doi: http://dx.doi.org/10.1175/2010BAMS3001.1.

Schlax, M. G., D. B. Chelton, and M. H. Freilich (2001). Sampling errors in wind fields constructed from single and tandem scatterometer datasets. *J. Atmos. Oceanic Technol.*, **18,** 1014–1036.

Stiles, B., and S. Yueh (2002). Impact of rain on wind scatterometer data. *IEEE Trans. Geosci. Remote Sensing*., **40**, 1973–1983.

Stoffelen, A. (1998). Toward the true near-surface wind speed: Error modeling and calibration using triple collocation. *J. Geophys. Res.*, **103,** 7755–7766.

Stoffelen, A., and D. Anderson (1997). Scatterometer data interpretation: Estimation and validation of the transfer function CMOD4. *J. Geophys. Res.,* **102**, 5767–5780.

Talagrand, O. (1997). Assimilation of observations, an introduction. *J. Met. Soc. Japan*, **75**, 191–209.

Talagrand, O. (1999). A posteriori verification of analysis and assimilation algorithms. *Proceedings of Workshop on Diagnosis of Data Assimilation Systems*, pp17-28. 2–4 November 1998, ECMWF, Reading, UK.

Vogelzang, J., A. Stoffelen, A. Verhoef, and J. Figa-Saldaña (2011).On the quality of high-resolution scatterometer winds. *J. Geophys. Res.*, **116**, C10033, doi:10.1029/2010JC006640.

Vogelzang, J., and A. Stoffelen (2012). NWP model error structure functions obtained from scatterometer winds. *IEEE Transactions on Geoscience and Remote Sensing,* **50**(7), 2525-2533.

Wahba, G., D. Johnson, F. Gao, and J. Gong (1995). Adaptative tuning of numerical weather prediction models: Randomized GCV in three- and four-dimensional data assimilation. *Mon. Wea. Rev.*, **123**, 3358–3369.

Weissman, D., M. A. Bourassa, and J. Tongue (2002). Effects of rain rate and magnitude on SeaWinds scatterometer wind speed errors. *J. Atmos. Oceanic Technol*., 19, 738–746.

Weissman, D. E., B. W. Stiles, S. M. Hristova-Veleva, D. G. Long, D. K. Smith, K. A. Hilburn, and W. L. Jones (2012). Challenges to Satellite Sensors of Ocean Winds: Addressing Precipitation Effects. *J. Atmos. Oceanic Technol.*, **29**, 356–374. doi: http://dx.doi.org/10.1175/JTECH-D-11-00054.1.

Yu, L., and X. Jin, (2012). Buoy perspective of a high-resolution global ocean vector wind analysis constructed from passive radiometers and active scatterometers (1987-present). *J. Geophys. Res*., **117**, C11013, doi:10.1029/2012JC008069.

Yueh, S. H., B. W. Stiles, W.-Y. Tsai, H. Hu, and W. T. Liu (2001). QuikSCAT geophysical model function for tropical cyclones and applications to Hurricane Floyd. *IEEE Trans. Geosci. Remote Sensing*, **39**, 2601–2612.

Figure Captions

Figure 1. (a) Selection of the optimal weight ratio based on two criteria, namely, the STD wind speed differences between the minimum of the cost function and buoy measurements (x-axis) and the STD wind speed differences between the minimum of the cost function and input satellite observations (y-axis). Each cross represents one experiment, with the corresponding weight ratio marked next to the cross. (b) Location of buoys used in the weight selection experiment.

Figure 2. Number of weight perturbation experiments versus the globally averaged STD weight assignment error in wind speed (red line), zonal wind component (black line), and meridional wind component (blue line) for year 2008.

Figure 3. The 25-year time-mean of the OAFlux wind fields and uncertainty estimates in response to the uncertainty in weight assignment. Left column: the annual mean fields of (a) wind speed, (b) zonal (positive eastward), and (c) meridional (positive northward) winds. Center column: the annual mean error fields of (d) wind speed, (e) zonal and (f) meridional winds. Right column: zonally averaged annual-mean values for (g) wind speed and associated error estimate, (h) zonal wind and associated error estimate, and (i) meridional wind and associated error estimate.

Figure 4. Same as Figure 3 but for time-mean January.

Figure 5. Same as Figure 3 but for time-mean July.

Figure 6. Averaged number of rain days per month constructed from SSM/I and SSMIS sensors (F13, F16, and F17) during the 1988-2012 period. (a) Annual mean, (b) January, and (c) July. Unit: number of days per month.

Figure 7. Averaged number of high-wind (>15ms^{-1}) days per month constructed from SSM/I and SSMIS sensors (F13, F16, and F17) during the 1988-2012 period. (a) Annual mean, (b) January, and (c) July. Unit: number of days per month.

Figure 8. Zonally averaged values for annual mean (thick black), January (blue), and July (red) over the 25-year period (1988-2012). (a) Rain days per month, (b) High wind days per month, (c) estimated error of wind speed, (d) estimated error of zonal wind, and (e) estimated error of meridional wind.

Figure 9. Case study of daily-mean fields from satellite observations on 01 January 2005. (a) rain rate from SSM/I F13, (b) wind speed from SSM/I F13, and (c) wind speed from QuikSCAT.

Figure 10. Case study of the OAFlux daily-mean winds and associated error estimates on 01 January 2005. (a) wind speed, (b) zonal wind, (c) meridional wind, (d) estimated error of wind speed, (e) estimated error of zonal wind, and (f) estimated error of meridional wind.

Figure 11. (a) Annual-mean averaged rain rate in 2008 derived from SSM/I F13, (b) the total number of rain days in 2008 constructed from SSM/I F13, and (c) the total number of rain days in 2008 from QuikSCAT.

Figure 12. The total number of high-wind days in 2008 constructed from (a) SSM/I F13 and (b) QuikSCAT.

Figure 13. Increase of the wind speed error with (a) SSM/I F13 rain rate and (b) SSM/I F13 wind speed constructed from daily-mean fields in 2008.

(a)

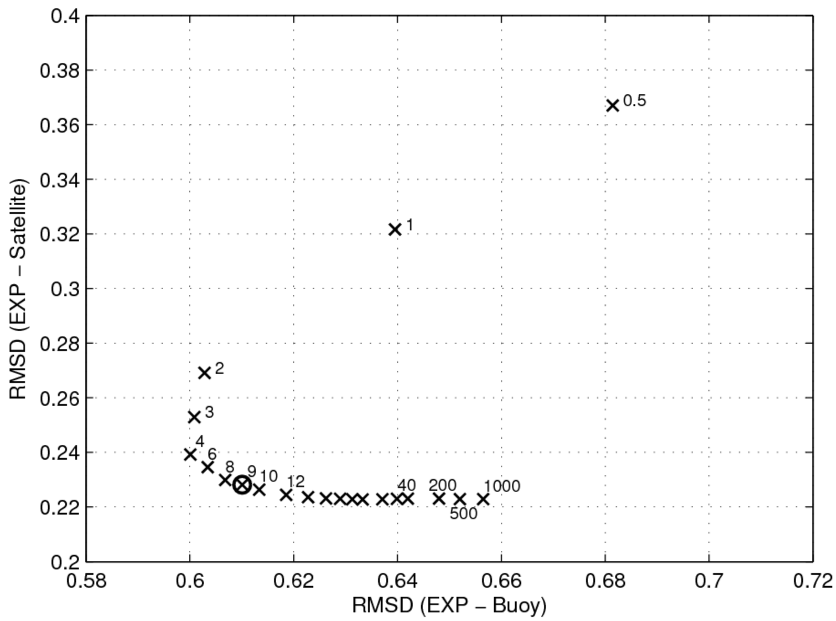

(b)

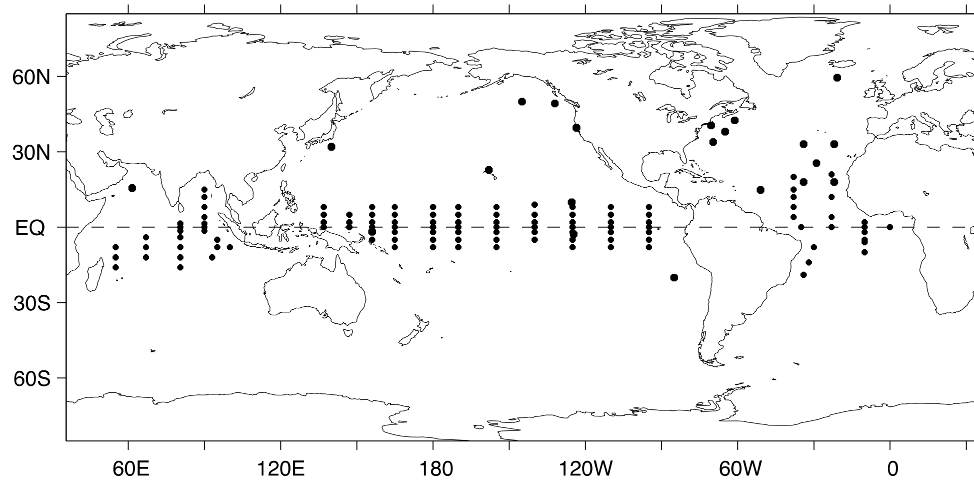

Figure 1. (a) Selection of the optimal weight ratio based on two criteria, namely, the STD wind speed differences between the minimum of the cost function and buoy measurements (x-axis) and the STD wind speed differences between the minimum of the cost function and input satellite observations (y-axis). Each cross represents one experiment, with the corresponding weight ratio marked next to the cross. (b) Location of buoys used in the weight selection experiment.

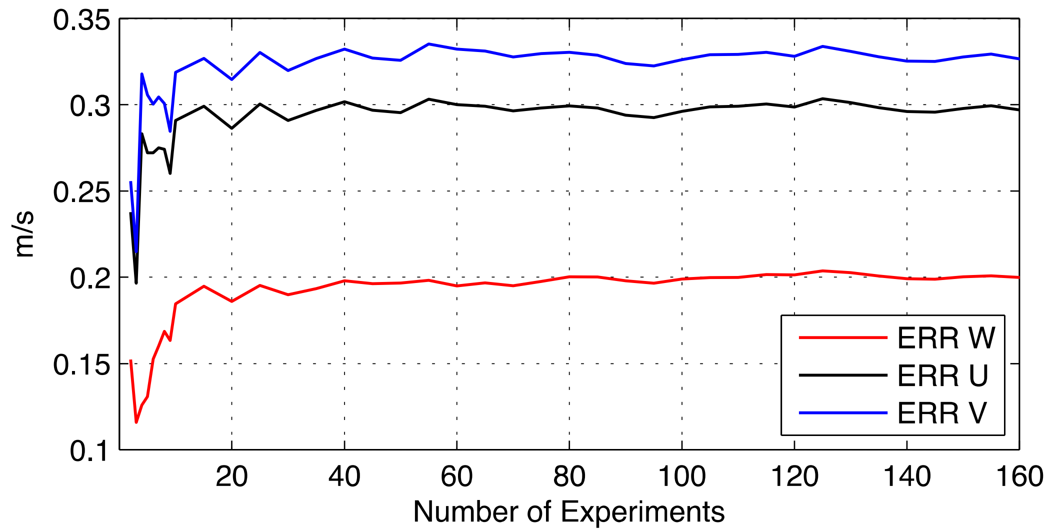

Figure 2. Number of weight perturbation experiments versus the globally averaged STD weight assignment error in wind speed (red line), zonal wind component (black line), and meridional wind component (blue line) for year 2008.

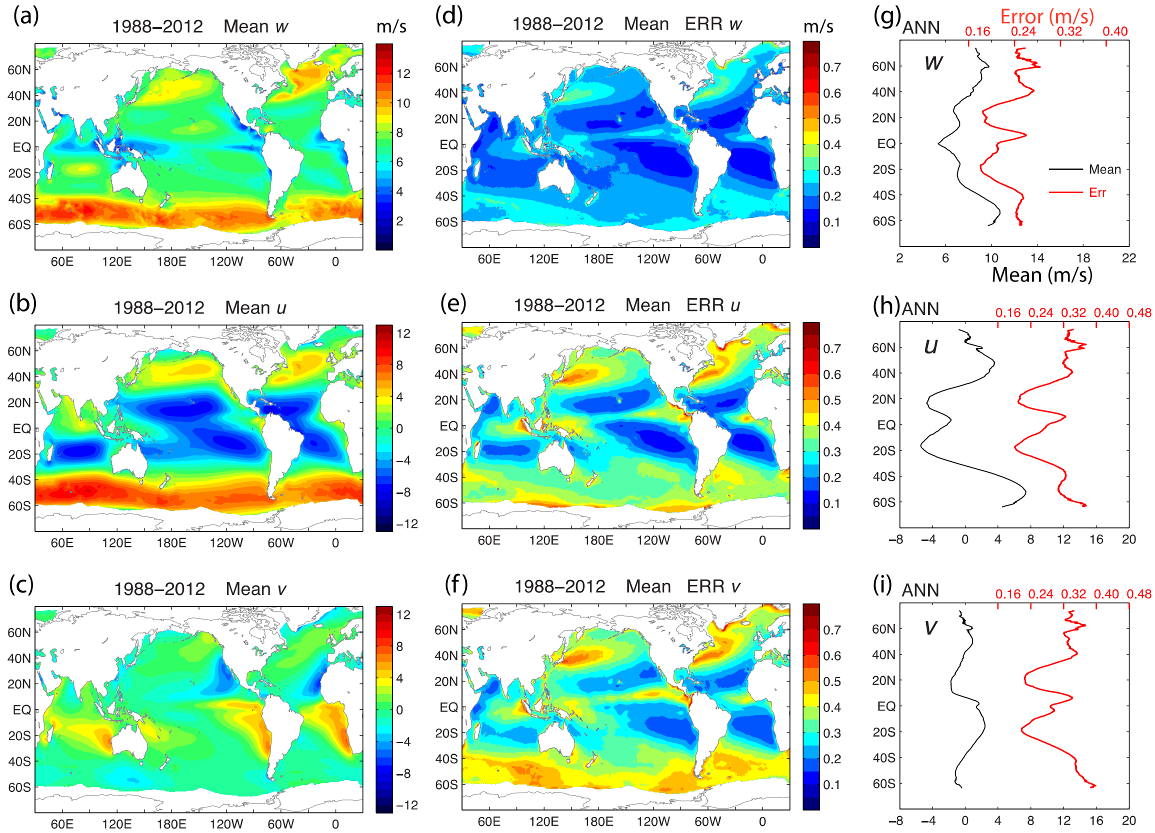

Figure 3. The 25-year time-mean of the OAFlux wind fields and uncertainty estimates in response to uncertainty in weight assignment. Left column: the annual mean fields of (a) wind speed, (b) zonal (positive eastward), and (c) meridional (positive northward) winds. Center column: the annual mean error fields of (d) wind speed, (e) zonal and (f) meridional winds. Right column: zonally averaged annual-mean values for (g) wind speed and associated error estimate, (h) zonal wind and associated error estimate, and (i) meridional wind and associated error estimate.

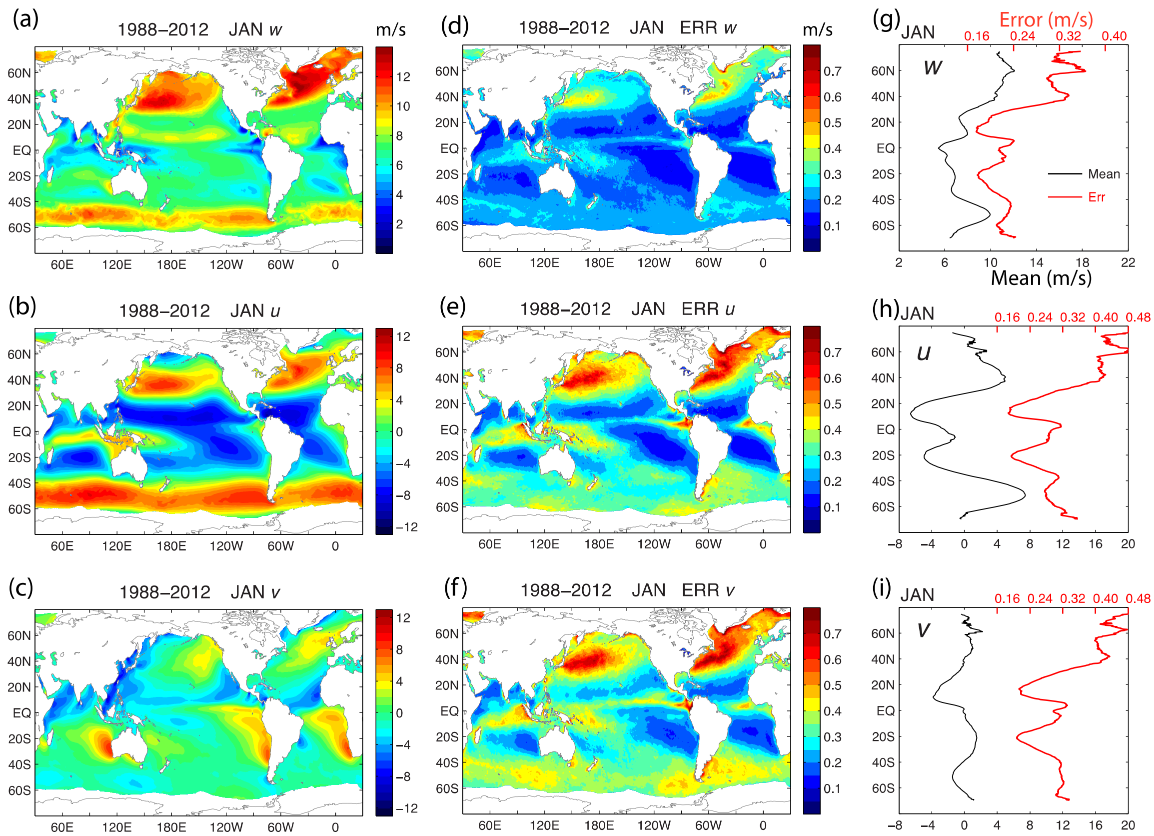

Figure 4. Same as Figure 3 but for time-mean January.

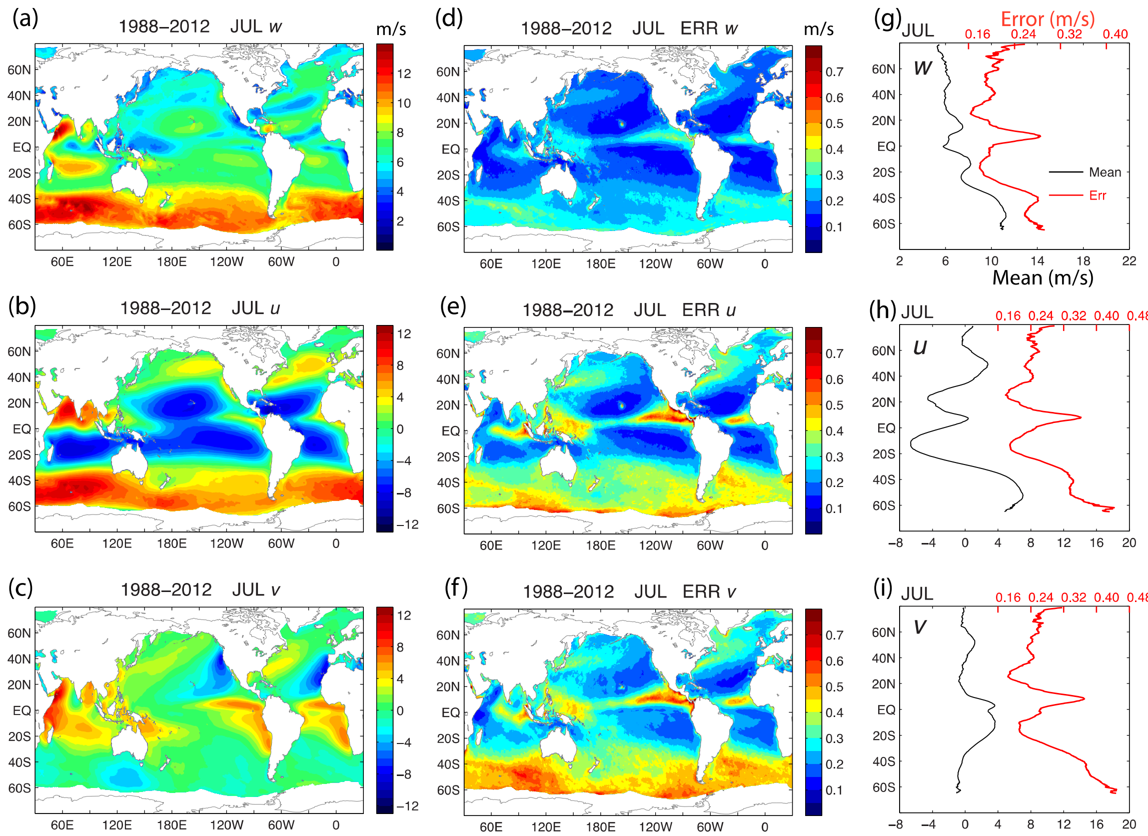

Figure 5. Same as Figure 3 but for time-mean July.

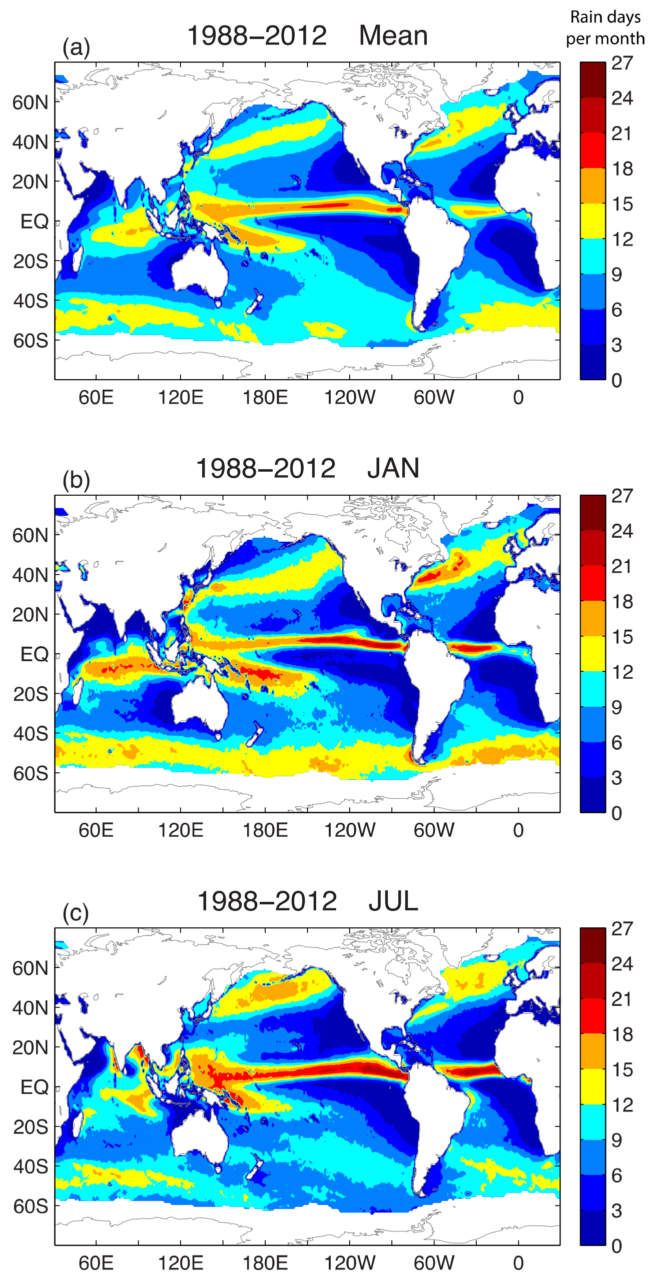

Figure 6. Averaged number of rain days per month constructed from SSMI/SSMIS sensors (F13, F16, and F17) during the 1988-2012 period. (a) Annual mean, (b) January, and (c) July. Unit: number of days per month.

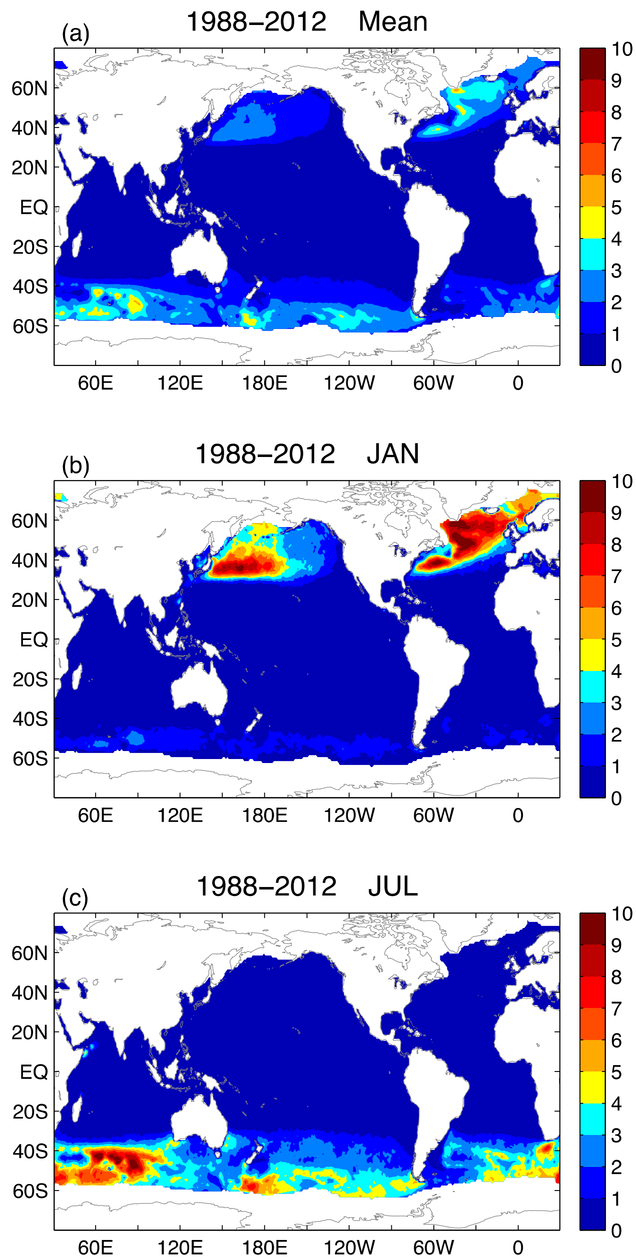

Figure 7. Averaged number of high-wind (>15ms^{-1}) days per month constructed from SSM/I and SSMIS sensors (F13, F16, and F17) during the 1988-2012 period. (a) Annual mean, (b) January, and (c) July. Unit: number of days per month.

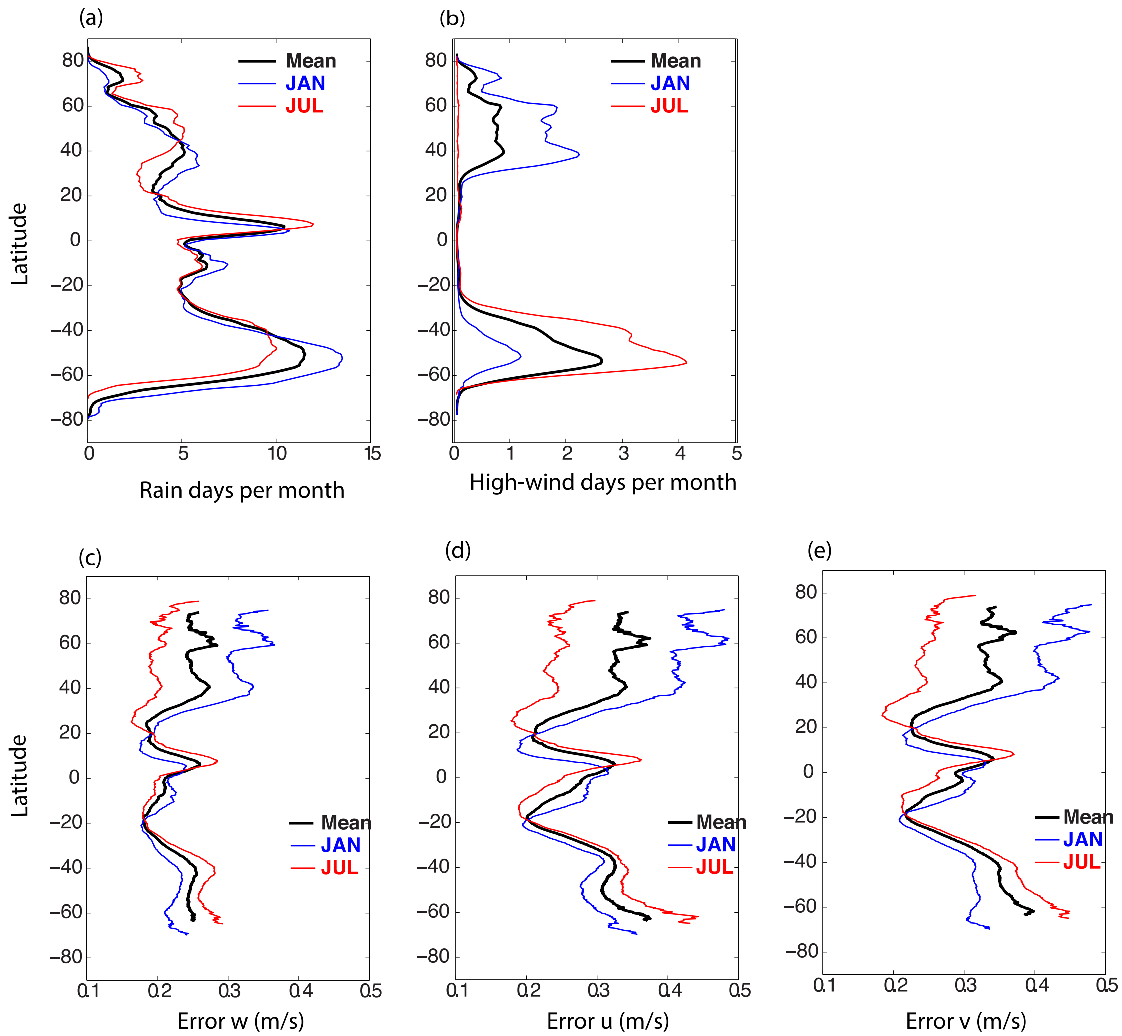

Figure 8. Zonally averaged values for annual mean (thick black), January (blue), and July (red) over the 25-year period (1988-2012). (a) Rain days per month, (b) High wind days per month, (c) estimated error of wind speed, (d) estimated error of zonal wind, and (e) estimated error of meridional wind.

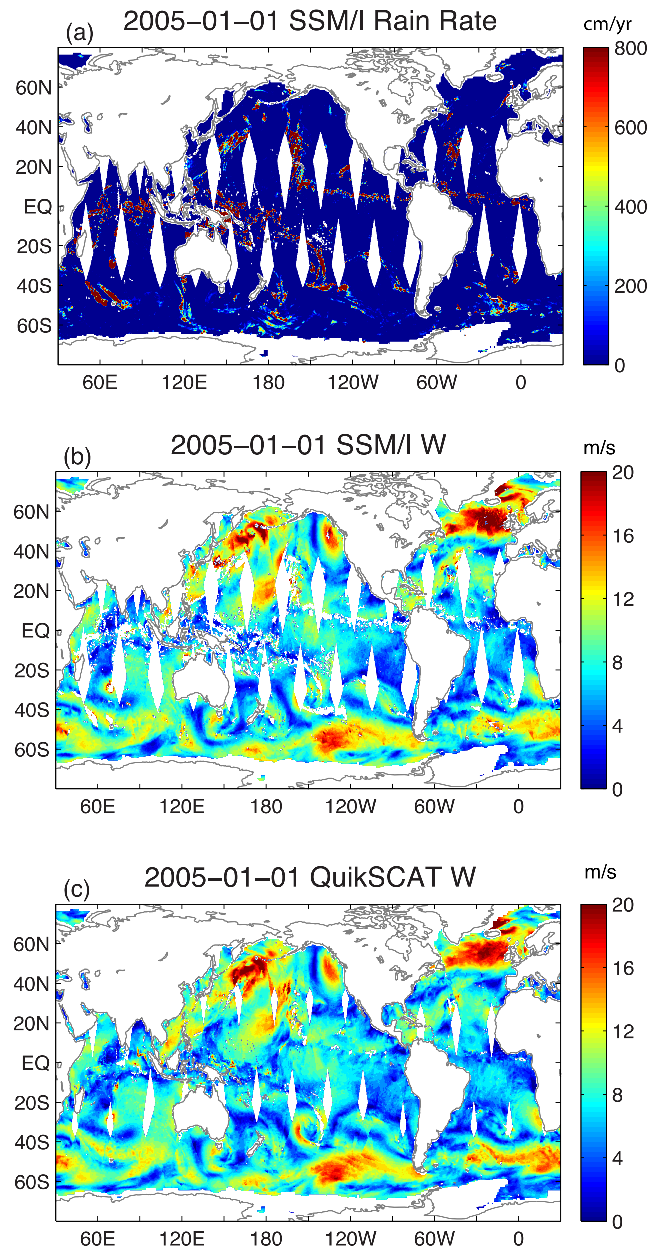

Figure 9. Case study of daily-mean fields from satellite observations on 01 January 2005. (a) rain rate from SSM/I F13, (b) wind speed from SSM/I F13, and (c) wind speed from QuikSCAT.

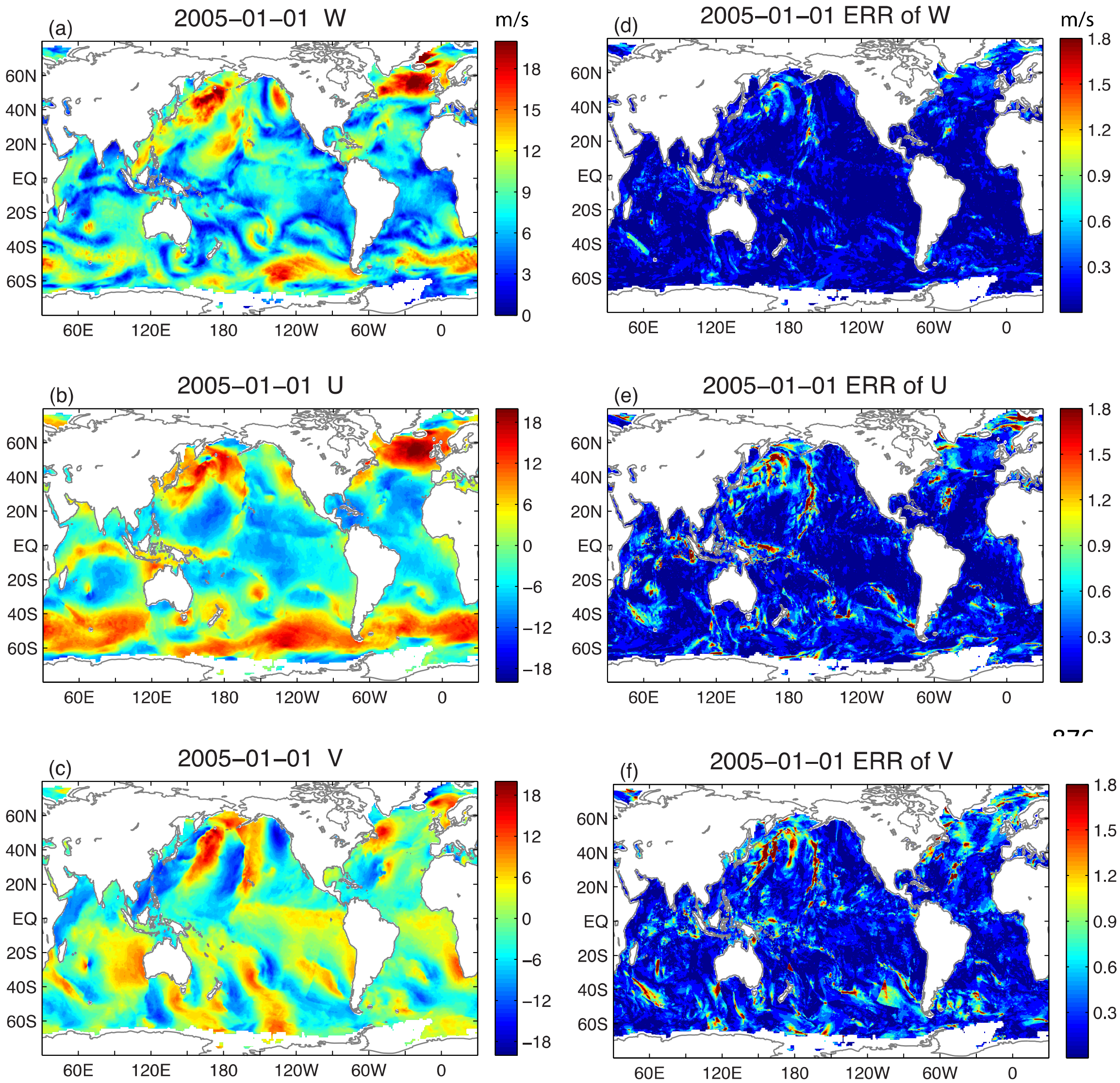

Figure 10. Case study of the OAFlux daily-mean winds and associated error estimates on 01 January 2005. (a) wind speed, (b) zonal wind, (c) meridional wind, (d) estimated error of wind speed, (e) estimated error of zonal wind, and (f) estimated error of meridional wind.

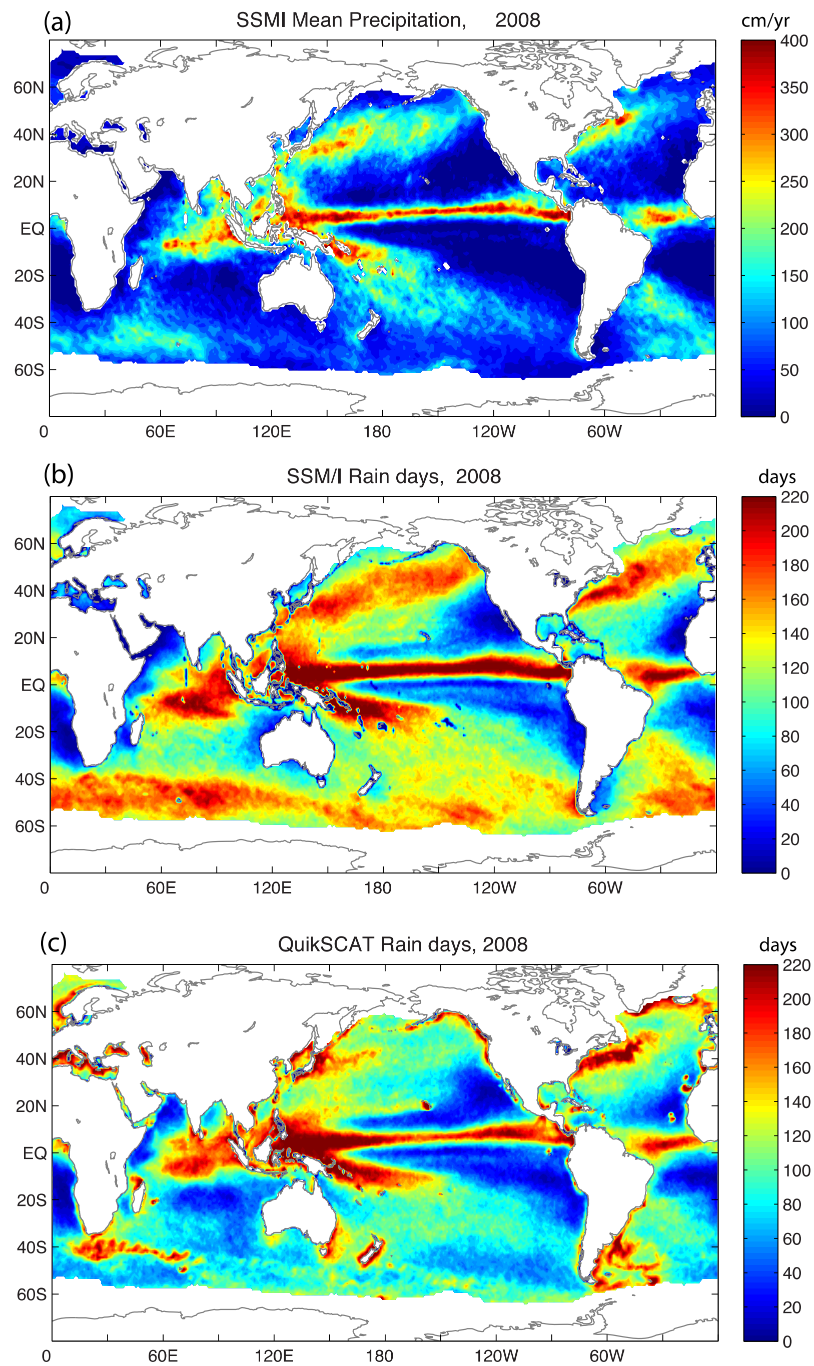

Figure 11. (a) Annual-mean averaged rain rate in 2008 derived from SSM/I F13, (b) the total number of rain days in 2008 constructed from SSM/I F13, and (c) the total number of rain days in 2008 from QuikSCAT.

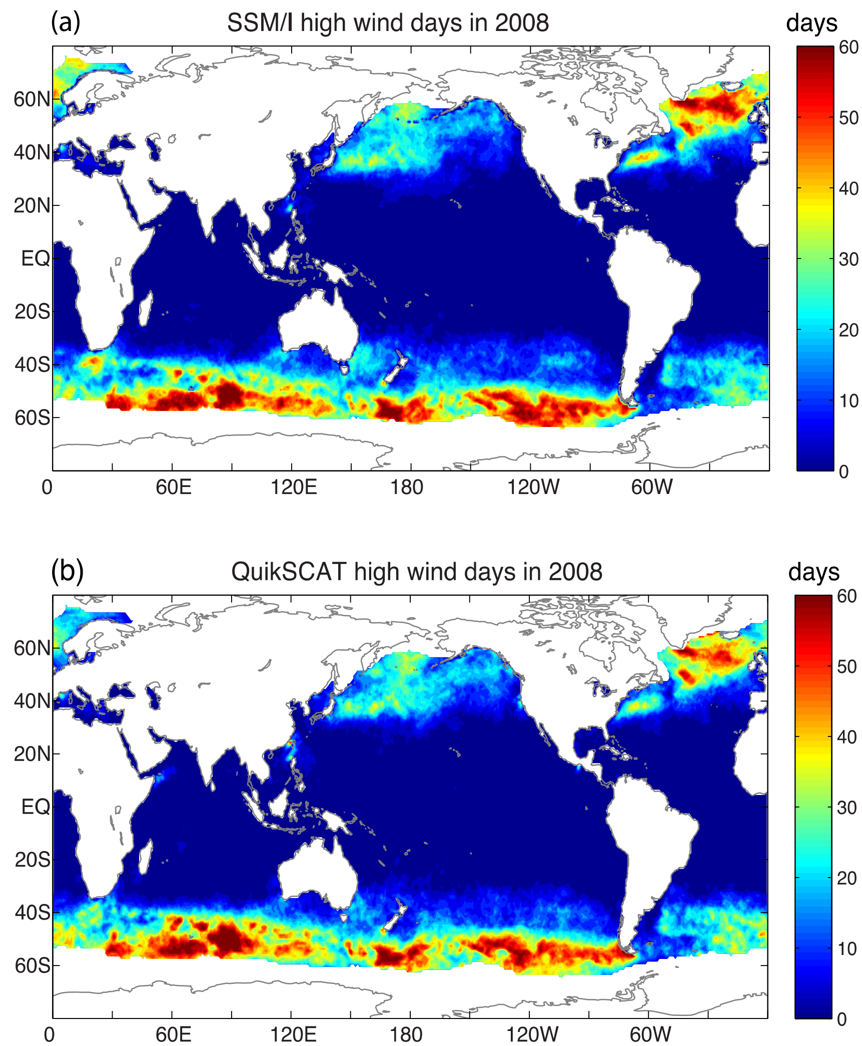

Figure 12. The total number of high-wind days in 2008 constructed from (a) SSM/I F13 and (b) QuikSCAT.

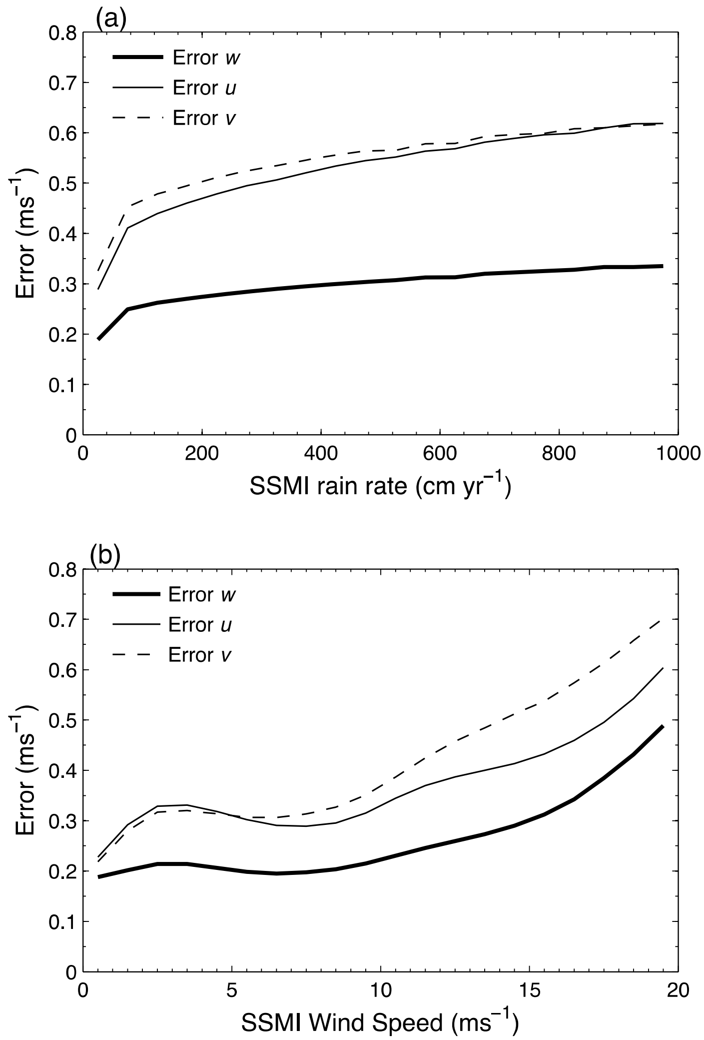

Figure 13. Increase of the wind speed error with (a) SSM/I F13 rain rate and (b) SSM/I F13 wind speed constructed from daily-mean fields in 2008.